nature methods

BRIEF COMMUNICATION

https://doi.org/10.1038/s41592-019-0663-9

An adaptive excitation source for high-speed multiphoton microscopy

Bo Li*, Chunyan Wu, Mengran Wang, Kriti Charan and Chris Xu*

Optical imaging is important for understanding brain function. However, established methods with high spatiotemporal resolution are limited by the potential for laser damage to living tissues. We describe an adaptive femtosecond excitation source that only illuminates the region of interest, which leads to a 30-fold reduction in the power requirement for two- or three-photon imaging of brain activity in awake mice for improved high-speed longitudinal neuroimaging.

High imaging speed is necessary for recording the activity of a large number of neurons[1–7]. Because typical multiphoton microscopes (MPMs) operate in the photon-shot-noise-limited regime, the maximum number of neurons that can be imaged at high spatial and temporal resolution is fundamentally limited by the maximum permissible average and peak power in biological specimens. Increasing the scanning speed cannot overcome the limit imposed by the 'photon budget', because a certain number of signal photons per second per neuron is needed in order to quantify the neuronal activity with a high confidence level. An effective approach to improve the imaging speed is to only image the region of interest (ROI)[8–10] or multiple ROIs. Since the ROI (for example, the labeled neurons) may occupy a small fraction of the volume of the mouse brain, a large improvement in imaging speed can be achieved by

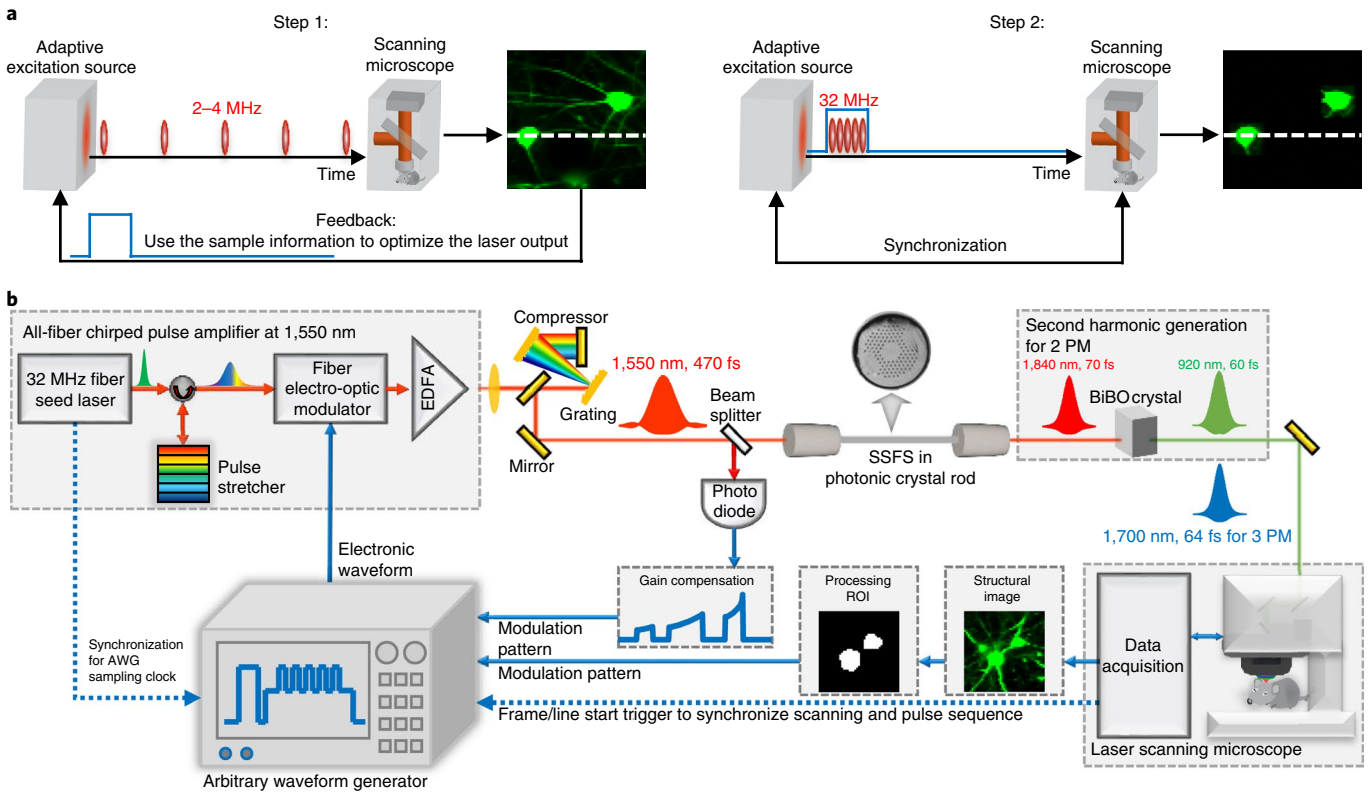

Fig. 1 | The AES for MPMs. a, Working principle. The creation of the AES consists of two steps: (1) a high-resolution structural image is obtained by raster scanning of the sample, and the image is processed to find the ROIs, for example, the neurons; and (2) an adaptive pulse train is generated on the basis of the ROI information. The synchronization of the scanning and the pulse sequence ensures that the excitation beam only illuminates the ROIs. **b**, Experimental set-up. The optical path is shown in red and green, and the electrical path is shown in blue. The measured second-order autocorrelation traces are shown at three locations along the optical path. The full width at half maximum of the pulse width (assuming squared hyperbolic secant (sech)^2 intensity profiles) is indicated next to the autocorrelation traces. BIBO crystal, bismuth triborate crystal.

School of Applied and Engineering Physics, Cornell University, Ithaca, New York, USA. *e-mail: bl627@cornell.edu; chris.xu@cornell.edu

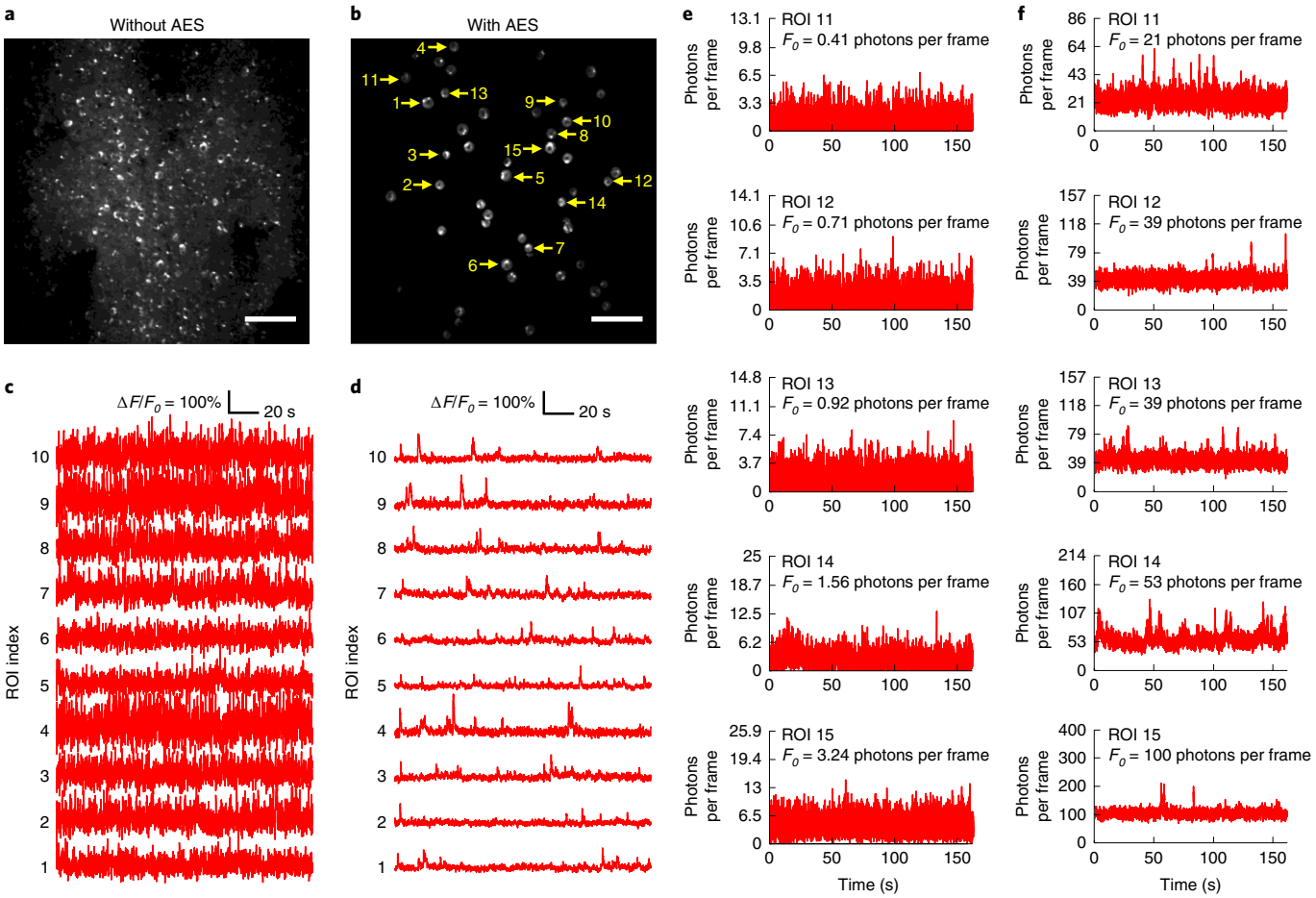

Fig. 2 | Comparison of 3PM of the spontaneous activity of neurons without and with AES at the same location in an awake mouse. The neurons are located at 750 µm beneath the dura and labeled with jRGECO1a (red fluorescent calcium indicator protein). **a**, Structural image of neurons without AES. **b**, Structural image of neurons with AES. **c**,**d**, Spontaneous activity traces recorded from the labeled neurons indicated in **b** in neurons without (**c**) and with (**d**) AES. **e**,**f**, Quantitative photon counting of the activity traces of the neurons recorded from the labeled neurons indicated in **b** in neurons without (**e**) and with (**f**) AES. The images have a FOV of 620 × 620 µm with 512 × 512 pixels per frame. Scale bars, 100 µm. *F, fluorescence intensity; F_0,* baseline fluorescence; *ΔF, F-F_0*.

illuminating only the ROIs, as compared with conventional raster scanning.

We developed a laser source that will adapt to the sample under study (that is, an adaptive excitation source, AES) for high-speed imaging of a large number of neurons at low light-exposure level. Figure 1a,b shows the principle and the detailed experimental set-up of a MPM with the AES for recording neuronal activity. A high-resolution structural image is obtained by raster scanning of the sample, and the image is processed to find the ROIs. For recording the activity of the neurons, for example, the bright regions of the somas define the ROIs. The ROI information is first converted to a digital binary sequence in the time domain and then fed to an arbitrary waveform generator (AWG), which drives a fiber-integrated electro-optic modulator (EOM) and encodes the ROI information onto the pulse pattern. The pulse train (now matched to the sample under study) is amplified to high pulse energy and launched into the laser scanning MPM. The synchronization of scanning and the pulse sequence ensures that the excitation beam will only illuminate the ROIs. By allocating all the permissible laser power on the ROIs (that is, the laser is completely 'turned off' outside the ROIs), the signal generation, and therefore the imaging speed, is improved by the inverse of the volume fraction of the ROIs, without increasing the average or peak power on the sample. A salient feature of our design is that the 'unwanted' pulses are removed before the final power amplifier (that is, the erbium-doped fiber amplifier, EDFA) stage. While modulation of laser power has been done routinely in the past, for example, by blanking the beam or enhancing the dynamic range, the modulation was always performed after the laser or amplifier output (that is, outside the excitation source)[2,11]. Even though the same adaptive pulse pattern could be obtained by modulation after the laser output, more than 30 times higher output power would be required from the laser (Fig. 2 and Supplementary Note 1), making the system impractical. In addition, by placing the modulator inside the excitation source, our design allows a high-speed and low-power (only needs to handle <100 mW) fiber-optic modulator to perform the intensity modulation.

Because it is tailored to match the ROIs of the sample under study, the pulse pattern is no longer periodic in time. The main challenge for the AES is to overcome the gain transient in the EDFA, similar to what occurs for burst-mode amplification in telecom and fiber-optic systems[12], as illustrated in Supplementary Fig. 1a, before compensation. To equalize the intensity of the output pulses, we setup an automatic feedback loop to precompensate the gain transient (Fig. 1b, Supplementary Figs 1 and 2 and Supplementary Video 1). The intensity of the output pulses is measured by a photodiode (PD). On the basis of the measured optical waveform, the AWG output (that is, the modulation pattern) is adjusted to pre-shape the input pulse train to the EDFA. This process is repeated until the

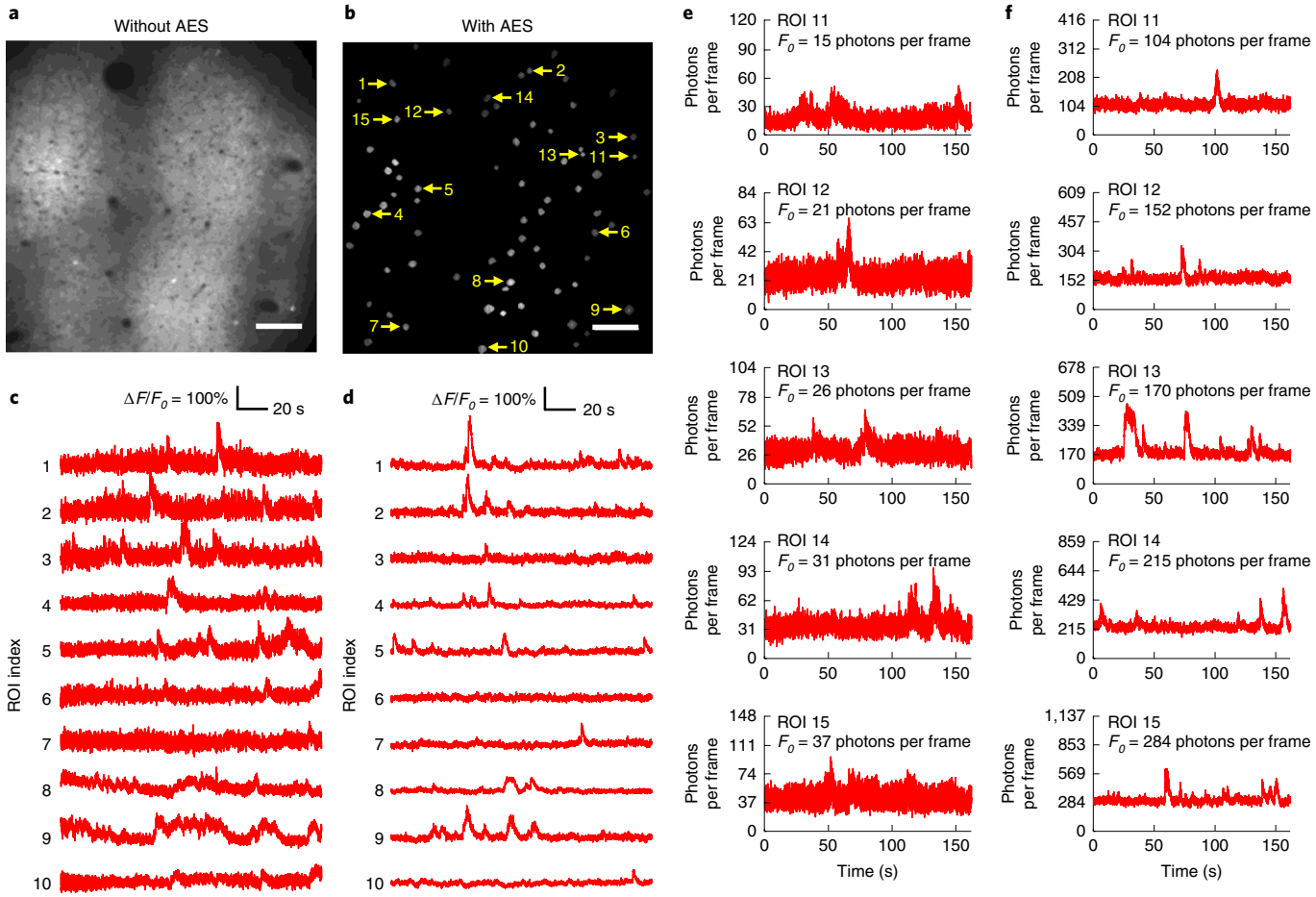

Fig. 3 | Comparison of 2PM of the spontaneous activity of neurons without and with AES at the same location in an awake mouse. The neurons are located at 680 µm beneath the dura and labeled with the calcium indicator GCaMP6s. **a**, Structural image of neurons without AES. **b**, Structural image of neurons with AES. **c**,**d**, Spontaneous activity traces recorded from the labeled neurons indicated in **b** in neurons without (**c**) and with (**d**) AES. **e**,**f**, Quantitative photon counting of the activity traces of the neurons recorded from the labeled neurons indicated in **b** in neurons without (**e**) and with (**f**) AES. The images have a FOV of 700 × 700 µm with 512 × 512 pixels per frame. Scale bars, 100 µm.

pulse-to-pulse intensity fluctuation is sufficiently reduced. The input and output of the EDFA after different numbers of iterations are shown in Supplementary Fig. 1b. As shown in Supplementary Fig. 1c, the root-mean-squared (RMS) fluctuation of the pulse intensity at the output of the EDFA decreases with the number of iterations. After 30 iterations, which took a total of approximately 15 s to complete, the RMS fluctuation decreased from ~17% to ~0.005%. The intensity-equalized pulse train is then launched into a photonic crystal rod and undergoes soliton self-frequency shift. The output at 1,700 nm is used for three-photon microscopy (3PM), and the solitons at 1,840 nm are frequency-doubled to 920 nm for two-photon microscopy (2PM).

3PM requires high pulse energy (for example, ~ 1 nJ at the focus). Because the maximum average power in biological specimens is limited by sample heating, the repetition rate of the laser for 3PM is typically low (for example, at 1 to 2 MHz), making 3PM incompatible with high-speed imaging. To demonstrate the improved imaging speed enabled by the AES, we performed in vivo 3PM in a densely labeled transgenic mouse. jRGECO1a-labeled neurons in an awake mouse (7 months old, similar data for $n = 9$ mice) were imaged at 750 µm beneath the dura with a FOV of 620 µm × 620 µm and a frame rate of 30 Hz (512 × 512 pixels per frame) (Fig. 2, Supplementary Figs. 3–8 and Supplementary Videos 2 and 3). A comparison of 3PM of neuronal activity with and without AES at the same location is shown in Fig. 2. The ROIs were designed to be somewhat larger than the neurons in order to compensate for the motion of the awake mouse (Supplementary Fig. 3 and Supplementary Videos 2 and 3). The photon number per neuron per frame with the AES is more than 30 times higher than that without the adaptive excitation scheme, although the same average power of 35 mW is used. More fluorescence time traces are shown in Supplementary Fig. 4. The total recording time was 60 min (Supplementary Fig. 5 and Supplementary Video 4). Since the ROIs occupy ~4.2 % of the FOV and the fill fraction of the resonant scan is 71.3% in the temporal domain (see Methods), more than 30 times reduction in the average excitation power is achieved; that is, an average power of approximately 1.2 W would be required to obtain the same traces if we had used a conventional laser at 32 MHz repetition rate. We performed a longitudinal study and recorded from the same neurons in an awake jRGECO1a mouse (12–17 weeks old, male) on 6 different days over a period of 4 weeks (Supplementary Figs. 6 and 7). We carried out immunostaining of the brains after imaging and confirmed that there was no measurable tissue damage (Supplementary Fig. 8). The performance demonstrated that the AES enables fast three-photon activity imaging, and overcomes a substantial weakness in 3PM.

We also performed in vivo 2PM of the activity of GCaMP6s-labeled neurons[13] in an awake mouse (7 months old, similar data for $n = 2$ mice) at 680 µm beneath the dura with a FOV of

700 µm × 700 µm and a frame rate of 30 Hz (512×512 pixels per frame). A comparison of 2PM of neuronal activity with and without AES at the same location is shown in Fig. 3. The photon number per neuron per frame with the adaptive excitation is more than 7 times higher than that without the adaptive excitation, even though the average power used for adaptive excitation is ~4.5 times lower. More fluorescence time traces are shown in Supplementary Fig. 9 and Supplementary Video 5. For ROI imaging with the AES, the average power at the surface of the brain was 18 mW. Since the ROIs occupy ~3 % of the FOV and the fill fraction of the resonant scan is 71.3% in the temporal domain, an average power of approximately 800 mW would be required to obtain the same traces if we had used a conventional laser at 32 MHz repetition rate. Such a high average power is beyond the thermal damage threshold (typically ~ 200 mW at 920 nm) of the mouse brain[14]. The demonstrated imaging performance cannot be obtained by external modulation of a conventional femtosecond laser (for example, the Ti:Sapphire laser) because an average power of ~3 W would be required at 920 nm. Such a power level is beyond the reach of existing two-photon excitation sources (Supplementary Note 1).

While imaging neural activity is the focus of this paper, the ROI can be other structures, such as the blood vessels (Supplementary Fig. 10 and Supplementary Videos 6 and 7).

Three-dimensional random-access MPM (RAMP) using acousto-optic deflectors (AOD)[15–18] is capable of performing random-access ROI imaging of populations of neurons within scattering tissues. To achieve the performance at which only the ROIs are illuminated, however, gating of the laser output is still necessary, particularly when the pixel dwell time is comparable to the pixel transit time of the AOD scanner[17]. Therefore, the AES can be combined with RAMP to further improve the excitation efficiency of the system. On the other hand, RAMP suffers from several shortcomings, such as a complicated dispersion compensation scheme and low deflection efficiency of the AOD (for example, about 75% for each AOD at ~800 nm, and even lower for longer wavelengths owing to material limitations[17]). A comparison between AES and AOD microscopy is presented in Supplementary Note 2, and shows that imaging with the AES can substantially outperform the best random-access, point-scanning, AOD system when the number of ROIs is large. Another major advantage of the AES is that it can be integrated with any existing laser-scanning MPM as long as the pixel clock of the microscope is accessible. For example, we show in Supplementary Fig. 11 structural and ROI imaging of neurons and dendrites using the AES and a commercially available MPM (FV1000MPE, Olympus). No modification of the microscope hardware or software was necessary for performing the experiments.

The low average power used in achieving the imaging results (for example, 18 mW for 2PM and 35 mW for 3PM) indicates that there is plenty of power budget to further increase the imaging speed using the AES, for example, by using higher speed resonant scanners or polygon scanners. While we have demonstrated imaging of a single plane using the AES, it can be straightforwardly applied to three-dimensional volumetric imaging by combining it with high-speed axial scanning devices, such as remote focusing[19,20], opening up exciting new opportunities for high-speed, large-scale, volumetric imaging of neuronal activity with cellular resolution.

We demonstrated an AES for imaging neuronal activity with a large FOV, a large penetration depth and a high frame rate while using low average power. Although our main motivation is to improve the speed of activity recording, the concept of the AES represents a new direction in designing an imaging system in which the excitation source itself is optimized according to the sample under study. The adaptive excitation technique requires no modification of the microscope hardware, has the same large FOV as a conventional MPM, and works at the excitation wavelengths for both 2PM and 3PM. In fact, the AES can be integrated with any existing MPMs, which will enable straightforward translation of the technique to the wider imaging community.

Online content

Any methods, additional references, Nature Research reporting summaries, source data, extended data, supplementary information, acknowledgements, peer review information; details of author contributions and competing interests; and statements of data and code availability are available at https://doi.org/10.1038/s41592-019-0663-9.

Received: 8 October 2018; Accepted: 24 October 2019;
Published online: 2 December 2019

References

1. Denk, W., Strickler, J. H. & Webb, W. W. Two-photon laser scanning fluorescence microscopy. *Science* **248**, 73–76 (1990).
2. Zipfel, W. R., Williams, R. M. & Webb, W. W. Nonlinear magic: multiphoton microscopy in the biosciences. *Nat. Biotechnol.* **21**, 1369–1377 (2003).
3. Helmchen, F. & Denk, W. Deep tissue two-photon microscopy. *Nat. Meth.* **2**, 932–940 (2005).
4. Dombeck, D. A., Khabbaz, A. N., Collman, F., Adelman, T. L. & Tank, D. W. Imaging large-scale neural activity with cellular resolution in awake, mobile mice. *Neuron.* **56**, 43–57 (2007).
5. Horton, N. G. et al. In vivo three-photon microscopy of subcortical structures within an intact mouse brain. *Nat. Photon.* **7**, 205–209 (2013).
6. Sofroniew, N. J., Flickinger, D., King, J. & Svoboda, K. A large field of view two-photon mesoscope with subcellular resolution for in vivo imaging. *eLife* **5**, e14472 (2016).
7. Ouzounov, D. G. et al. In vivo three-photon imaging of activity of GCaMP6-labeled neurons deep in intact mouse brain. *Nat. Meth.* **14**, 388–390 (2017).
8. Papagiakoumou, E. et al. Scanless two-photon excitation of channelrhodopsin-2. *Nat. Meth.* **7**, 848–854 (2010).
9. Packer, A. M., Russell, L. E., Dalgleish, H. W. P. & Häusser, M. Simultaneous all-optical manipulation and recording of neural circuit activity with cellular resolution in vivo. *Nat. Meth.* **12**, 140–146 (2014).
10. Pnevmatikakis, E. A. et al. Simultaneous denoising, deconvolution, and demixing of calcium imaging data. *Neuron* **89**, 285–299 (2016).
11. Yang, R., Weber, T. D., Witkowski, E. D., Davison, I. G. & Mertz, J. Neuronal imaging with ultrahigh dynamic range multiphoton microscopy. *Sci. Rep.* **7**, 5817 (2017).
12. Desurvire, E., Giles, C. R. & Simpson, J. R. Gain saturation effects in high-speed, multichannel erbium-doped fiber amplifiers at lambda = 1.53 µm. *J. Lightwave Tech.* **7**, 2095–2104 (1989).
13. Chen, T.-W. et al. Ultrasensitive fluorescent proteins for imaging neuronal activity. *Nature* **499**, 295–300 (2013).
14. Podgorski, K. & Ranganathan, G. Brain heating induced by near-infrared lasers during multiphoton microscopy. *J. Neurophysiol.* **116**, 1012–1023 (2016).
15. Reddy, G. D., Kelleher, K., Fink, R. & Saggau, P. Three-dimensional random access multiphoton microscopy for functional imaging of neuronal activity. *Nat. Neurosci.* **11**, 713–720 (2008).
16. Grewe, B. F., Langer, D., Kasper, H., Kampa, B. M. & Helmchen, F. High-speed in vivo calcium imaging reveals neuronal network activity with near-millisecond precision. *Nat. Meth.* **7**, 399–405 (2010).
17. Katona, G. et al. Fast two-photon in vivo imaging with three-dimensional random-access scanning in large tissue volumes. *Nat. Meth.* **9**, 201–208 (2012).
18. Chavarha, M. et al. Fast two-photon volumetric imaging of an improved voltage indicator reveals electrical activity in deeply located neurons in the awake brain. Preprint at *bioRxiv* https://doi.org/10.1101/445064 (2018).
19. Botcherby, E. J. et al. Aberration-free three-dimensional multiphoton imaging of neuronal activity at kHz rates. *Proc. Natl Acad. Sci. USA* **109**, 2919–2924 (2012).
20. Weisenburger, S. et al. Volumetric Ca^{2+} imaging in the mouse brain using hybrid multiplexed sculpted light microscopy. *Cell* **177**, 1050–1066 (2019).

Methods

Fiber-based AES for 3PM. The source consists of a fiber chirped-pulse amplification system at 1,550 nm, and a photonic crystal rod for soliton self-frequency shift (SSFS). A compact, turnkey, fiber-based seed laser (FPL-02CFFT, Calmar) delivered linearly polarized pulses with an average power of 100 mW, a repetition rate of 32 MHz and a bandwidth (full width at half maximum (FWHM)) of 13.7 nm at 1,550 nm. The pulses were then chirped to 642 ps, with second-order dispersion of –51 ps per nm and third-order dispersion of –2.6 ps per nm^2. A fiber-integrated electro-optic modulator (IOAP-MOD9170-F-F-0, SDL) was used to modulate the chirped pulses according to the ROIs of the sample under study. The adaptive pulses were amplified by a two-stage home-built EDFA and compressed by a grating pair (PC 1200 30×110×16 NIR, Spectrogon). The compressed output has a pulse width of 470 fs (Fig. 1) and an average power of more than 6 W. SSFS was performed in a 44-cm-long, polarization-maintained photonic crystal rod (SC-1500/100-Si-ROD, NKT Photonics) with an effective mode area of 4,400 μm^2 at 1,550 nm. After collimation, a 1,620-nm long-pass filter (BLP01-1648R-25, Semrock) was used to filter out the residual pump. The soliton was shifted to 1,680 nm at an input pulse energy of 1,300 nJ (ref. [21]). The pulse width of the soliton was measured to be 64 fs by second-order autocorrelation, assuming a sech^2 intensity profile (Fig. 1). The pulse energy of the soliton was 140 nJ. A silicon wafer (uncoated, 2-mm thick, Edmund Optics) is positioned at the Brewster's angle to precompensate the dispersion of the microscope optics. The intensity stability of the soliton pulses was measured using a two-photon excited photocurrent in a silicon PD. The RMS fluctuation of the soliton pulses was less than 1% when measured for 10 min at a sampling rate of 100 kHz. The wavelength stability is measured using a spectrometer. The RMS fluctuation of the center wavelength of the soliton is less than 1 nm when measured for 20 min at 2 wavelength scans per s.

Fiber-based AES for 2PM. The same fiber chirped-pulse amplification system at 1,550 nm was used as the pump for SSFS. SSFS was performed in a 36-cm-long, polarization-maintained photonic crystal rod (DC-200-70-PM-Yb-ROD, NKT Photonics) with an effective mode area of 2,300 μm^2 at 1,550 nm. After collimation, a 1,720 nm long-pass filter (1720LP/50.8, Omega optical) was used to filter out the residual pump. The soliton was shifted to 1,840 nm, at an input pulse energy of 1,260 nJ. The pulse width of the soliton was measured to be 70 fs by performing second-order autocorrelation, assuming a sech^2 intensity profile (Fig. 1). The pulse energy of the soliton was 110 nJ. Pulses at the wavelength of 920 nm were then obtained by second harmonic generation (SHG) of the soliton source, using a frequency-doubling crystal bismuth borate ($\theta = 9.8°$ (the polar angle relative to the optical axis), $\varphi = 0°$ (the azimuthal angle in the optical plane), L = 1 mm; Castech). The pulse energy and pulse duration of the pulses at 920 nm were 60 nJ and 60 fs, respectively. A prism pair (80-cm separation, 10SF10, Newport) was used to precompensate the dispersion of the microscope optics. The intensity stability of the SHG pulses was measured using a two-photon excited photocurrent in a GaAsP PD. The RMS fluctuation of the SHG pulses was less than 1% when measured for 10 min at a sampling rate of 100 kHz.

Feedback loop for compensating the gain transient of the EDFA. A small portion (<1%) of the light at 1,550 nm after the grating pair was detected by a PD (ET08CFC, Thorlabs). The PD output was low-pass filtered (BBLP-39+, Mini-Circuits) and recorded by a data-acquisition card (ATS9371, Alazar Technologies). On the basis of the measured output optical waveform, the AWG (NI PXI-5412, National Instruments) output was adjusted to preshape the input pulse train to the EDFA. This process was repeated until the pulse-to-pulse intensity fluctuation was sufficiently reduced. The algorithm for adjusting the modulation pattern of the AWG is: $A_{n+1} = A_n \times (1 - C \times (P_n - \langle P \rangle) / \langle P \rangle)$, where P_n is the measured peak power of an output pulse of the nth iteration, $\langle P \rangle$ is the averaged peak power of all output pulses of the nth iteration, A_n is the AWG modulation amplitude of the nth iteration, A_{n+1} is the AWG modulation amplitude of the $(n+1)$th iteration, and $C \in (0,1)$ is a constant. 20 to 30 iterations were typically used to equalize the pulse intensity.

Imaging setup. The images were taken with a custom-built multiphoton microscope with a high-numerical aperture objective (Olympus XLPLN25XWMP2, 25×, NA1.05). The signal was epicollected through the objective and then reflected by a dichroic beam splitter (FF705-Di01, Semrock) to the detectors. We used two PMTs with GaAsP photocathodes (H7422P-40, Hamamatsu) for the fluorescence and third-harmonic generation (THG) signals. For 2PM, the optical filter for the fluorescence signal was centered at 520 nm (FF01-520/60-25, Semrock). For 3PM, a 568-nm dichroic beam splitter (MD568, Thorlabs) was inserted at 45° to the signal beam path to separate the fluorescence and the THG signal to their respective PMTs. The filters for the fluorescence and THG signal were centered at 630 nm (MF630-69, Thorlabs) and 550 nm (FF01-550/49-25, Semrock), respectively. The mouse was placed on a motorized stage (MP-28, Sutter Instrument). A computer running the ScanImage 5.3 module (Vidrio Technologies) with MATLAB (MathWorks) software was used to control the stage translation and image acquisition. The PMT current was converted to voltage by transimpedance amplifiers (DHPCA-100, Femto, and TIA60, Thorlabs). Analog-to-digital conversion was performed by a data acquisition card (NI5734, National Instruments). For depth measurement, the slightly larger index of refraction in brain tissue (1.35 to 1.43 for the cortex), relative to water (~1.33), results in an underestimate (5–10%) of the actual imaging depth within the tissue because the imaging depths reported here are the raw axial movement of the objective. A galvo-resonant scanner (RESSCAN-GEN, Sutter Instrument) was used to achieve the frame rate of 30 Hz at 512×512 pixels per frame.

Comparison of 3PM of neuronal activity with and without AES. For 3PM without AES, the average power is 35 mW below the objective lens, and the excitation source outputs a uniform, periodic pulse train with a repetition rate of 2 MHz. For 3PM with AES, the average power is also 35 mW. The repetition rate of the pulses within the ROIs (that is, when the laser is 'on') was 32 MHz, sufficient for high-speed recording of neuronal activity using the resonant scanner.

Comparison of 2PM of neuronal activity with and without AES. For 2PM without AES, the average power below the objective lens is 80 mW, and the excitation source outputs a uniform, periodic pulse train with a repetition rate of 4 MHz. For 2PM with AES, the average power is 18 mW. The repetition rate of the pulses within the ROIs (that is, when the laser is 'on') was 32 MHz, sufficient for high-speed recording of neuronal activity using the resonant scanner.

Fill fraction of the resonant scanner. For a resonant scanner, the angular velocity at the edge of the scan field is low and highly nonlinear, and thus, the acquisition is inactive and no pixel is recorded in this region. The ratio between the active acquisition time and the total time of a line is defined as the fill fraction in ScanImage 5.3. In the experiment, the fill fraction was 71.3% in the temporal domain and 90% in the spatial domain. The AES was turned off (that is, no output pulses) in the inactive regions for data acquisition.

Synchronization of the laser, electro-optical modulation and microscope. For synchronization, there are two clocks, one from the seed laser source and the other from the resonant scanner of the microscope. The synchronization output of the pulsed seed laser (32 MHz) was used as the sampling clock of the AWG, ensuring synchronization of the laser pulses and the electro-optical modulation. The third harmonic of the synchronization output of the seed laser (that is, 96 MHz) was used as the sampling clock of the microscope data acquisition. According to the ROI information obtained from the structural image (512×512 pixels), 512 binary digital sequences (each sequence corresponds to one line of a frame) were generated by MATLAB and stored in the on-board memory of the AWG. The line clock from the microscope was used as the start trigger of the AWG so that the laser scanning and the electro-optical modulation were synchronized. For activity recording, the repetition rate of the excitation source within the ROI was 32 MHz. For structural imaging, a uniform periodic pulse train with a repetition rate of 4 MHz and 2 MHz was used for 2PM and 3PM, respectively. A large number of frames (~3,000) were averaged to achieve the high signal-to-noise ratio of the structural images.

Image processing for structural imaging and activity recording. Structural images were processed with a median filter of 1- to 2-pixel radius and then normalized by linear transform of pixel intensities to saturate the brightest 0.2–3% of pixels in each frame. Fluorescence intensity (F) traces were low-pass filtered with a hamming window of a time constant of 0.23 s. All traces with absolute photon counts were raw data without filtering. We determined the baselines of the traces (F_0) by excluding the transients. $\Delta F/F$ traces were then obtained according to the formula $(F - F_0) / F_0$.

Photon counting. To show the absolute signal strength in the unit of photon count rate, pixel values are multiplied by a calibration factor. The calibration factor is obtained by observing the modes in the histogram of images of a uniform fluorescein sample, recorded with a short pixel dwell time such that each pixel typically has one photon or zero photons.

Animal procedures. All animal experiments and housing procedures were conducted in accordance with Cornell University Institutional Animal Care and Use Committee guidance. We used transgenic CamKII-tTA/tetO-GCaMP6s mice (7 months old, male) for 2PM, transgenic C57BL/6J-Tg(Thy1-jRGECO1a) GP8.58Dkim/J mice (3–7 months old, male) for 3PM of neurons and C57BL/6J mice (3 months old, male) for 3PM of blood vessels.

Chronic craniotomy. The diameter of the cranial window is 5 mm. For 2PM and 3PM of blood vessels, the window was centered at 2.5 mm lateral and 2 mm posterior from the bregma point. For 3PM of neurons, the window is centered at the bregma point. To reduce the tissue growth under the window for chronic imaging, we used a coverslip assembly consisting of a donut-shaped coverslip (inner diameter, 4.5 mm; outer diameter, 5.5 mm; laser cut by Potomac Photonics) glued concentrically above a 5 mm diameter coverslip (#1 thickness, Electron Microscopy Sciences; optical glue, Norland Optical Adhesive 68). The circular coverslip fit snugly into the open cranial window and was placed directly onto the intact dura. The donut coverslip on the top was glued to the skull (3 M Vetbond tissue adhesive) to keep the 5-mm coverslip pressed against the tissue, displacing as much room for potential tissue growth as possible. We applied multiple thin layers of metabond glue on the exposed skull surrounding the coverslip and positioned the head-bar directly onto the glue. The head-bar was further stabilized with

Metabond glue and dental cement covering the skull and the circular coverslip. For all mice, chronic imaging was performed at least 5 d after the surgery for tissue inflammation to disappear, with the animal kept alive after each imaging session. For awake imaging, the mouse was standing in a slippery tube when the head was fixed on a custom-made stereotaxic plate using the metal head-bar holder.

Statistics and reproducibility. For 3PM of brain activity (Fig. 2, Supplementary Figs. 3–5 and Supplementary Videos 2–4), similar results were obtained from 9 mice (3–7 months old). Longitudinal recording of neuronal activity (Supplementary Figs. 6 and 7) was from 1 mouse (12–17 weeks). For immunohistology (Supplementary Fig. 8), similar results were obtained from 6 mice (3–7 months old). For 2PM of brain activity (Fig. 3, Supplementary Fig. 9 and Supplementary Video 5), similar results were obtained from 2 mice (3 and 7 months old). For compensation of the gain transient (Supplementary Figs. 1 and 2 and Supplementary Video 1), similar results were obtained for more than 30 different image patterns. For 3PM of blood flow (Supplementary Fig. 10 and Supplementary Videos 6 and 7), similar results were obtained from 2 mice (both 3 months old). 2PM of neurons with a commercial MPM (Supplementary Fig. 11) was from 1 mouse (2 months old).

Reporting Summary. Further information on research design is available in the Nature Research Reporting Summary linked to this article.

Data availability

The data that support the findings of this study are available from the corresponding author upon reasonable request.

Code availability

The MATLAB code for driving the AWG (NI PXI-5412, National Instruments) and data-acquisition card (ATS9371, Alazar Technologies) can be found at https://github.com/Bo-Li-ORCID-0000-0003-1492-0919/Adaptive-excitation-source-for-high-speed-multi-photon-microscopy.

References

21. Charan, K., Li, B., Wang, M., Lin, C. P. & Xu, C. Fiber-based tunable repetition rate source for deep tissue two-photon fluorescence microscopy. *Biomed. Opt. Express* **9**, 2304–2311 (2018).

Acknowledgements

We thank members of the Xu research groups (T. Wang, D. Ouzounov, D. Sinfeld, C. Huang, X. Yang, A. Mok, F. Xia, Y. Hontani, Y. Qin, N. Akbari, K. Choe, T. Ciavatti and C. Zhuang) for their help. We thank M. Buttolph and L. G. Wright for discussions. This work is partially funded by NIH/NINDS (grant no. U01NS090530 to C.X.), and the National Science Foundation NeuroNex (grant no. DBI-1707312 to C.X.).

Author Contributions

C.X. initiated and supervised the study. B.L. designed and performed the experiments and analyzed the data. K.C. contributed to the construction of the fiber amplifiers. C.W. set up the awake imaging system and performed immunohistology and most of the animal surgeries. M.W. performed some of the animal surgeries. B.L. and C.X. wrote the manuscript.

Competing interests

The authors declare no competing interests.

Additional information

Supplementary information is available for this paper at https://doi.org/10.1038/s41592-019-0663-9.

Correspondence and requests for materials should be addressed to B.L. or C.X.

Peer review information Rita Strack was the primary editor on this article and managed its editorial process and peer review in collaboration with the rest of the editorial team.

Reprints and permissions information is available at www.nature.com/reprints.

nature research

Corresponding author(s): Bo Li, Chris Xu

Last updated by author(s): Oct 11, 2019

Reporting Summary

Nature Research wishes to improve the reproducibility of the work that we publish. This form provides structure for consistency and transparency in reporting. For further information on Nature Research policies, see Authors & Referees and the Editorial Policy Checklist.

Statistics

For all statistical analyses, confirm that the following items are present in the figure legend, table legend, main text, or Methods section.

n/a	Confirmed
☐	☒ The exact sample size (*n*) for each experimental group/condition, given as a discrete number and unit of measurement
☐	☒ A statement on whether measurements were taken from distinct samples or whether the same sample was measured repeatedly
☒	☐ The statistical test(s) used AND whether they are one- or two-sided *Only common tests should be described solely by name; describe more complex techniques in the Methods section.*
☒	☐ A description of all covariates tested
☒	☐ A description of any assumptions or corrections, such as tests of normality and adjustment for multiple comparisons
☒	☐ A full description of the statistical parameters including central tendency (e.g. means) or other basic estimates (e.g. regression coefficient) AND variation (e.g. standard deviation) or associated estimates of uncertainty (e.g. confidence intervals)
☒	☐ For null hypothesis testing, the test statistic (e.g. *F*, *t*, *r*) with confidence intervals, effect sizes, degrees of freedom and *P* value noted *Give P values as exact values whenever suitable.*
☒	☐ For Bayesian analysis, information on the choice of priors and Markov chain Monte Carlo settings
☒	☐ For hierarchical and complex designs, identification of the appropriate level for tests and full reporting of outcomes
☒	☐ Estimates of effect sizes (e.g. Cohen's *d*, Pearson's *r*), indicating how they were calculated

Our web collection on statistics for biologists contains articles on many of the points above.

Software and code

Policy information about availability of computer code

Data collection	Scan Image S5.3 for home-made microscope and Commercial software (FV10-ASW, Ver.02.01) for Olympus FV1000 MPM were used for collection of images. MATLAB 2017A was used for operation of the feedback loop, including arbitrary waveform generator and data acquisition card.
Data analysis	Fiji-ImageJ (version 2.0.0-rc-44/1.50e) was used for basic batch image operation (e.g. averaging, linear contrast stretch). MATLAB 2017A was used for basic batch image operations (e.g. averaging, linear contrast stretch, neuron segmentation); processing of activity traces (e .g. background determination, normalization).

For manuscripts utilizing custom algorithms or software that are central to the research but not yet described in published literature, software must be made available to editors/reviewers. We strongly encourage code deposition in a community repository (e.g. GitHub). See the Nature Research guidelines for submitting code & software for further information.

Data

Policy information about availability of data

All manuscripts must include a data availability statement. This statement should provide the following information, where applicable:

- Accession codes, unique identifiers, or web links for publicly available datasets
- A list of figures that have associated raw data
- A description of any restrictions on data availability

The data that support the findings of this study are available from the corresponding author upon request.

Field-specific reporting

Please select the one below that is the best fit for your research. If you are not sure, read the appropriate sections before making your selection.

☒ Life sciences ☐ Behavioural & social sciences ☐ Ecological, evolutionary & environmental sciences

For a reference copy of the document with all sections, see nature.com/documents/nr-reporting-summary-flat.pdf

Life sciences study design

All studies must disclose on these points even when the disclosure is negative.

Sample size	The proposed technique is a novel excitation source, with each pulse can be arbitrarily turned "on" and "off". The excitation performance does not depend on the sample size. We demonstrate mouse brain imaging. The repeated number for each figure is given in the "statistics and reproducibility" section.
Data exclusions	The baselines of the traces (F0) is defined as the lower 20%-40% of each trace during the whole recording time.
Replication	We performed experiments on different animals with different fluorescent dyes (GCaMP6, jRGECO1a, Texas red) and using different types of microscopes (home-made microscopes with either galvo-resonant scanners or galvo-galvo scanners, commercial Olympus FVIO00 MPM microscope), and they all work well.
Randomization	No group was allocated in this study, and any experiment involving comparison of imaging methods was done on the same animal during the same imaging session.
Blinding	Not applicable, since no group was allocated.

Reporting for specific materials, systems and methods

We require information from authors about some types of materials, experimental systems and methods used in many studies. Here, indicate whether each material, system or method listed is relevant to your study. If you are not sure if a list item applies to your research, read the appropriate section before selecting a response.

Materials & experimental systems

n/a	Involved in the study
☒	☐ Antibodies
☒	☐ Eukaryotic cell lines
☒	☐ Palaeontology
☐	☒ Animals and other organisms
☒	☐ Human research participants
☒	☐ Clinical data

Methods

n/a	Involved in the study
☒	☐ ChIP-seq
☒	☐ Flow cytometry
☒	☐ MRI-based neuroimaging

Animals and other organisms

Policy information about studies involving animals; ARRIVE guidelines recommended for reporting animal research

Laboratory animals	For in vivo 2PM with GCaMP6s, we used transgenic mice crossed from Tg(tetOGCaMP6s) 2Niell/J (The Jackson Laborary) and CaMKll-tTA (The Jackson Laboratory). We imaged 2 male. The age at the time imaging was ~7 months old. For in vivo 3PM with jRGECOla, we used transgenic mice C57BL/6J-Tg(Thyl-jRGECOla)GP8.S8Dkim/J (The Jackson Laborary). We imaged 9 male. The age at the time imaging was 3-7 months old. For in vivo 3PM with Texas red, we used wild type mice C57BL/6J (The Jackson Laborary). We imaged 2 male. The age at the time imaging was ~3 months old. For proof-of-concept imaging using commercial Olympus microscope, we used transgenic mice (B6.Cg-Tg(Thyl-YFPH)2Jrs/J; male; adult; the Jackson Laboratory; n=l, age= 8 weeks old).
Wild animals	This study did not involve any wild animals.
Field-collected samples	This study did not involve samples collected from the field.
Ethics oversight	All animal experiments and housing procedures were conducted in accordance with Cornell University Institutional Animal Care and Use Committee guidance.

Note that full information on the approval of the study protocol must also be provided in the manuscript.